CRYSTAL GROWTH & DESIGN

pubs.acs.org/crystal

Article

Influence of Hydrogen/Fluorine Substitution on Structure, Thermal Phase Transitions, and Internal Molecular Motion of Aromatic Residues in the Crystal Lattice of Steroidal Rotors

Tomasz Pawlak,* Dorota Czajkowska-Szczykowska, Izabella Jastrzebska, Rosa Santillan, Barbara Seroka, Jadwiga Maj, Jacek W. Morzycki, Pablo Labra-Vázquez, Norberto Farfán, Grzegorz D. Bujacz, and Marek J. Potrzebowski*

Cite This: *Cryst. Growth Des.* 2020, 20, 2202−2216

Read Online

ACCESS | Metrics & More | Article Recommendations | Supporting Information

ABSTRACT: Two, acyclic (**1**) and cyclic (**2**), steroidal molecular rotors containing 1,4-diethynyl-2,3-difluoro-phenylene units as rotators were investigated by means of single crystal X-ray diffraction, high resolution solid state NMR spectroscopy, and computer methods. The aim of this study was to understand and search for a correlation between the size of difluoro-phenylene units and free space in the crystal lattice required for molecular reorientation as well as the topology and time scale of dynamic processes. As a primary tool for analysis of molecular motions in the solid state, $^{1}H-^{13}C$ PISEMA, a technique which allows following the dynamics in the range of $10^{-3}-10^{-6}$ s, was employed. The PISEMA data defining the $^{1}H-^{13}C$ dipolar couplings, whose values are sensitive to local motion, were confronted with ^{13}C CSA parameters. Our studies revealed that replacing hydrogen by fluorine in acyclic rotors has significant consequences for dynamic processes. In the case of hydrogen-substituted species, free rotation around the 1−4 axis of the benzene ring was proven. For fluorine derivatives **1**, only small amplitude wobbling of aromatic residues was observed. The only large amplitude reorientation, a so-called π-jump around the 1−4 axis, was observed during the phase transition related with solvent migration from the crystal lattice. For cyclic rotors (**2**) two crystallographic forms **2A** (triclinic, *P*1 space group) and **2B** (monoclinic, $P2_1$ space group) are established. The form **2B** containing a heptane molecule in the crystal lattice undergoes a thermal transition with large amplitude motion of building units of the steroidal frame. The high dynamics of the fluorinated rotator for **2A** is proven.

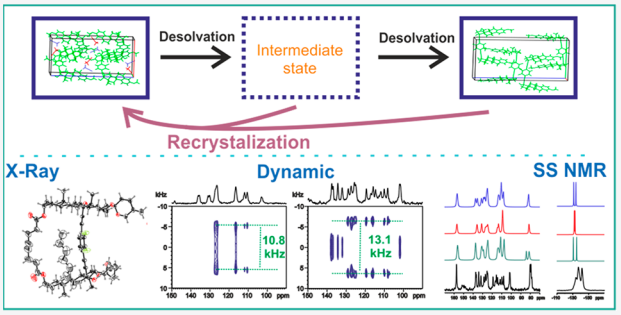

INTRODUCTION

One of the most challenging issues in modern science and technology is the development of strategies which allow, at the molecular level, the construction of materials with desired functions in the solid state. Among different sophisticated systems, molecular machines are examples of objects for which pure science, in a spectacular manner, is brought to practical application.[1−5] In the classical approach leading to the synthesis of species like the ones under discussion, the periodic rigid framework created by bulky groups called *stators* is covalently bound to a rotating fragment termed the *rotator*.[6−8] To date, a number of papers showing advanced methodologies for building molecular machines with properties similar to macroscopic mechanical objects have been published.[9−21]

The synthetic works have been focused on the procedures, whereby the main goal is chemical modification of the stator or variations in the structure of the rotator residue or both fragments using the same approach. Regardless the applied methodology used in the construction of molecular machines, at least one prerequisite has to be fulfilled. The low density is crucial for the design of mobile elements in solids, and this principle has been exploited in a variety of materials, the aim being to obtain new molecular mobility benchmarks. Further, the topology and time scale of molecular motion in the solid state is correlated with the presence of available space. In many cases this free volume contributes in few percent to the total volume, but it allows the dynamical moieties to achieve enough freedom.

Much effort has been devoted to develop synthetic procedures which allow chemical modification of the mobile part of molecular machines using simple and effective approaches.[22−24] The major motivation is constructing the

Received: September 6, 2019
Revised: February 19, 2020
Published: February 19, 2020

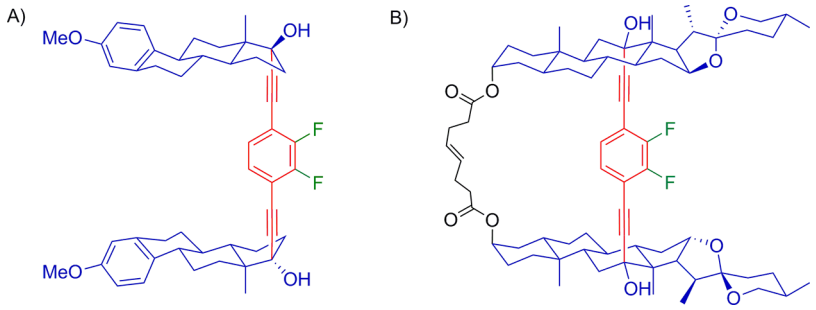

Figure 1. Molecular structures of **1** (A) and **2** (B).

dipole systems, sensitive to external stimuli. For instance, dipoles mounted on molecular rotors may lead to switchable organic ferroelectric materials. Concerted rotor dynamics of dipoles in regular environments can generate slow wave propagation in the radiofrequency regime, similar to acoustic waves, and can be used to build radio frequency filters. It is interesting to note that molecular rotors can interact with the diffusing chemical species (liquids, vapors, or gases). Through this chemical intervention, rotator speed can be modulated enabling a new generation of rotor-containing materials sensitive to guests. In principle, an applied electric field can be the stimulus for chemical release from porous materials. In contrast, when the molecular machine belongs to the group of host−guest complexes, the release of guest molecules from the crystal lattice can influence the dynamics of the dipolar rotator.

In this work, as part of our continuing interests in the synthesis and structural studies of chemically modified molecular rotors we report the X-ray, solid state, NMR, and computer analysis for 1,4-diethynylphenylene rotators connected by alkynylene moieties with steroidal frameworks.[25−29] The acyclic **1** and cyclic **2** steroidal molecular rotors shown in Figure 1 contain 1,4-diethynyl-2,3-difluoro-phenylene units as rotators.[26,30] Substitution of hydrogen by fluorine atoms produces derivatives, which fulfill the prerequisites for dipolar species.

The preliminary X-ray studies of **1** and **2** revealed that these systems can be defined as host−guest complexes. Further examination proved that these complexes are thermally unstable and the guest molecules are easily lost from the crystal lattice. The relationship between guest molecule migration, phase transitions, and local rotator dynamics seems to be a nontrivial question.

EXPERIMENTAL SECTION

Materials. The synthetic procedure for compound **1** has been reported elsewhere.[26]

Synthesis of Compound ***2***. Reagent-grade chemicals were purchased and used as received. Methylene chloride was freshly distilled. Flash column chromatography and dry flash chromatography were performed with silica gel, pore size 40 Å (70−230 mesh), unless otherwise stated. All reactions were monitored by TLC on silica gel plates 60 F_{254}. ^{1}H and ^{13}C NMR as well as FT-IR results confirming the structure of synthetic products can be found in the Supporting Information (SI).

Synthetic Procedure

(A) 12α-Ethynyl-25*R*-spirostane-3α,12β-diol 3-pent-4′-enoate (0.376 g, 0.7 mmol) was dissolved in dry THF (100 mL), then 2,3-difluoro-1,4-diiodobenzene (0.128 g, 0.35 mmol, 0.5 equiv), $Pd(PPh_3)_4$ (40 mg, 5 mol %), Cu_2I_2 (27 mg, 10 mol %), and DIPEA (2.5 mL) were added. The reaction mixture was stirred at reflux for 3 h. The solution was poured into aqueous solution of ammonium chloride and extracted with CH_2Cl_2. The organic layer was dried over Na_2SO_4 and concentrated under reduced pressure. The crude product was purified by liquid column chromatography (hexane−ethyl acetate 87:13), and 0.182 g (22%) of the diester as a white solid was obtained.

(B) To a solution of the obtained diester (30 mg, 0.025 mmol) in dry toluene (200 mL), second-generation Grubbs catalyst (6 mg, 0.007 mmol, 30 mol %) was added under argon. The reaction mixture was stirred for 1 h at 80 °C, then cooled down to room temperature, and quenched with ethyl vinyl ether (1 mL). The solvent was removed under reduced pressure.

Molecular structures of products of steps A and B are collected in the SI (Figures S1 and S2).

The separation of products (isomers *E* and *Z*) from the catalyst was performed by liquid column chromatography (hexane−ethyl acetate 9:1). The mixture of *E*/*Z* isomeric rotors **2E** and **2Z** was obtained (23 mg, 78% yield). The purification of the major *E* isomer was achieved by reversed-phase HPLC with a solvent mixture CH_3CN/CH_2Cl_2 (8:2).

X-ray Crystal Structure Determination. Single crystal diffraction experiment for **2** employing acetonitrile as solvent were carried out on Oxford SuperNova single-crystal diffractometer with micro source Cu Kα radiation (λ = 1.5418 Å) and a Titan detector. The plate crystal of dimensions 0.26 mm × 0.22 mm × 0.04 mm was glued to a glass capillary by epoxy glue and measured at room temperature. For low temperature data collection, the crystal has dimensions of 014 mm × 0.12 mm × 0.04 mm and was mounted to a capillary using vacuum grease. The absorption correction was performed based on the crystal shape, orientation, and absorption coefficient. Diffraction data collection, cell refinement, data reduction, and absorption correction were performed using the CrysAlis PRO program (Oxford Diffraction). The structure was solved by direct methods on SHELXS and refined using full-matrix least-squares methods on SHELX 2015 as implemented in the OLEX2 package.[31] The structure was validated by checkCIF (http://checkcif.iucr.org) and deposited to the Cambridge Crystallographic Data Centre (CCDC) under accession numbers 1817202 and 1950550 for low and 1950551 for room temperature structure. These crystal forms were named **2B**, **2A**, and **2Ar**. respectively.

Crystals of macrocyclic rotor **2** suitable for single-crystal X-ray diffraction studies were also obtained by room temperature evaporation of a saturated solution of ethyl acetate (or dichloromethane) and *n*-heptane. The intensity data were collected on an Enraf Nonius Kappa diffractometer with a CCD area detector ($\lambda_{MoK\alpha}$ = 0.71073 *A*°, monochromator:graphite) at 173 K. The crystals were mounted on conventional MicroLoops. All heavier atoms were found by Fourier map difference and refined anisotropically. All reflection data set were corrected for Lorentz and polarization effects. The first structure solution was obtained using the SHELXS-97 program and the SHELXL-97[32] was applied for refinement and output. All software manipulations were performed under the WinGX environment program set.[33] The programs Mercury 3.7 and ORTEP-3 were used to prepare artwork representations.[34,35] CCDC 1817202 contains the supplementary crystallographic data for this paper. These data can be

https://dx.doi.org/10.1021/acs.cgd.9b01179
Cryst. Growth Des. 2020, 20, 2202−2216

Scheme 1. Unit Cell Transformation of Structure 1

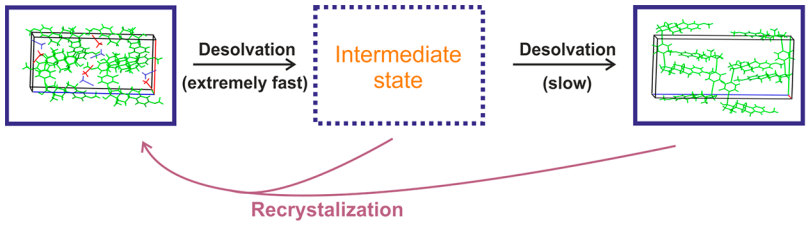

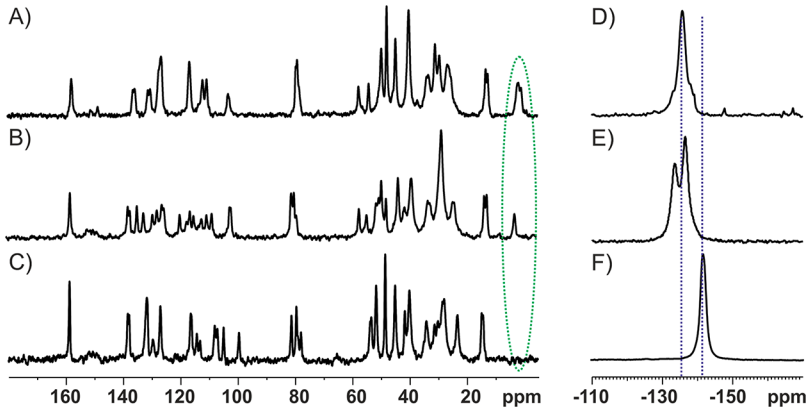

Figure 2. ^{13}C CP MAS NMR (A, B, C) and ^{19}F MAS NMR (D, E, F) spectra of **1**: Immediately after crystallization from acetonitrile−dichloromethane solvent mixture (A, D), after drying 2 h in the air (B, E) and after heating at 165 °C (C, F) recorded at ambient temperature with a spinning rate of 13 kHz (A, B, C) and 30 kHz (D, E, F).

obtained free of charge via https://summary.ccdc.cam.ac.uk/structure-summary-form (or from the Cambridge Crystallographic Data Centre, 12, Union Road, Cambridge CB2 1EZ, UK). This crystal form was named **2B**.

Solid-State NMR Experiments. The solid-state magic angle spinning (MAS) experiments were performed on a BRUKER Avance III 400 spectrometer (operating at 400.15, 376.52, and 100.61 MHz for ^{1}H, ^{19}F, and ^{13}C, respectively) equipped with a MAS probe head using 4 mm and 2.5 mm ZrO_2 rotors. The sample of glycine and polytetrafluoroethylene were used to set the Hartmann−Hahn condition for ^{13}C and ^{19}F, respectively. Adamantane (resonances at 38.48 and 29.46 ppm) was used as a secondary ^{13}C chemical-shift reference from external tetramethylsilane (TMS) in all experiments.[36]

The conventional $^{1}H \rightarrow {}^{13}C$ CP/MAS spectra were obtained with a proton 90° pulse length of 2.5 μs and contact time of 2 ms. For the single pulse ^{19}F MAS spectra, the 90° pulse length was 2.2 μs. The repetition delay varied from 5 to 25 s depending on the T_1 relaxation times of the measured nuclei in the particular sample. The FIDs were accumulated using a time domain size of 4 K with the spectral width 40 kHz for $^{1}H \rightarrow {}^{13}C$ CP/MAS. The RAMP shape pulse[37] was used during the cross-polarization and TPPM decoupling for $^{1}H \rightarrow {}^{13}C$ CP/MAS.[38]

For the $^{1}H-{}^{13}C$ PISEMA MAS experiment,[39] the ^{1}H effective field strength was 100 kHz in all of the experiments, and the ^{13}C spin-lock field strengths was adjusted to the first-order sideband condition, $\omega_{13C} = \omega_{1Heff} \pm \omega_r$. The spinning speed was 13 kHz and was regulated to ±3 Hz by a pneumatic control unit. Recycle delays were the same as for CP/MAS experiments. The 2D $^{1}H-{}^{13}C$ PISEMA MAS experiments incremented the SEMA contact time at a step of 16.28 μs. At a spinning speed of 13 kHz, the dwell time for the evolution period was 19.23 μs. The maximum t_1 evolution time was typically approximately 1 ms. Only cosine-modulated data were collected. Thus, a real Fourier transformation was performed on the t_1 data yielding spectra with a symmetrized ω_1 dimension and showing the dipolar splittings. Because the t_1 time signal increases with increasing SEMA contact time, the ω_1 dimension was processed using the baseline correction mode "qfil" in the TOPSPIN software, which subtracts a constant intensity from the time signals prior to the Fourier transformation yielding spectra free of a dominant zero-frequency peak giving the $^{1}H-{}^{13}C$ doublet. The $^{13}C-{}^{1}H$ FSLG HETCOR experiments were recorded with a proton 90° pulse length of 2.5 μs, contact time of 50 μs, repetition delay of 3 s, time domain size of 1024 data points in F2 and 64 data points in F1, and at a 13 kHz spinning rate.

A 5-π pulse 2D PASS scheme and 2000 Hz sample spinning speeds were used in the 2D experiments. The π-pulse length was 8 μs. Sixteen t_1 increments using the timings described by Antzutkin et al. were used in the 2D PASS experiments.[40] For each increment, 3072 scans were collected. Because the pulse positions in the t_1 set returned to their original positions after a full cycle and the t_1-FID formed a full echo, the 16-point experimental t_1 data were replicated to 256 points. Acquisition time was 80 h. After the Fourier transformation in the direct dimension, the 2D spectrum was sheared to align all side bands with the center bands in the indirect dimension of the 2D spectrum. One-dimensional chemical shift anisotropy (CSA) spinning sideband patterns were obtained from t_1 slices taken at the isotropic chemical shifts in the t_2 dimension of the 2D spectrum. The values of the principal elements of the CSA tensor were obtained from the best-fit simulated spinning sideband pattern. Simulations of the spinning CSA sideband spectra were performed on a PC using the Bruker TopSpin 3.0 program.[41]

The $^{1}H-{}^{13}C$ HETeronuclear CORrelation (invHETCOR) for indirect detection of ^{13}C experiments, described by Mao et al.,[42] were performed on a 600 MHz Avance III spectrometer (operating at 600.13 and 150.90 MHz for ^{1}H and ^{13}C, respectively) equipped with a MAS probe head using 1.3 mm ZrO_2 rotors. The following parameters were used: a 42 kHz spin rate, a proton 90° pulse length of 2.5 μs, a first contact time of 2 ms, a second contact time of 150 μs, and a proton π pulse (5 μs) in the middle of the evolution period (instead of CW ^{1}H decoupling as mentioned by Ishii and Tycko).[43] The maximal evolution times were $T1_{max}$ = 4.2 ms and $T2_{max}$ = 20 ms.

The values of the principal elements of the ^{19}F CSA tensor were obtained from the best-fit simulated spinning sideband pattern fitted to the 1D experimental ^{19}F spectra recorded with spinning rate of 10 kHz. Simulations of the spinning CSA sideband spectra were performed on a PC using the Bruker TopSpin 3.0 program.[41]

https://dx.doi.org/10.1021/acs.cgd.9b01179
Cryst. Growth Des. 2020, 20, 2202−2216

DFT Calculations in Periodic Boundary Conditions. The quantum chemical calculations were performed using the CASTEP code.[44,45] The geometry optimization was performed using the X-ray diffraction crystal structures of **1A**, **1B**, **2A**, and **2B** as an input file, and the generalized density approximation DFT functional PBE[46] was applied. A comparison of the average forces remaining on the atoms after geometry optimization was carried out for proton-only and all-atom (also with variable cell parameters) optimizations by using a maximum plane wave cutoff energy of 570 eV and ultrasoft pseudopotential.[47] We observed average forces (given as Cartesian components) up to ca. 0.01 (protons), 3.2 (carbon atoms), 1.6 (oxygen atoms), and 0.3 eV/Å (fluorine atoms) after proton-only optimization of the studied structures, which suggested that proton-only optimized structures are not the preferred structure at the considered level of theory. After all-atom optimizations the average forces were smaller (especially for heavy atoms) and had a similar magnitude for all atomic species that is ca. 0.005 (protons), 0.003 (carbon atoms), 0.003 (oxygen atoms), and 0.002 eV/Å (fluorine atoms), which clearly indicated that these structures are preferable and therefore they were considered during discussion of results. The unit cell parameters were taken from the X-ray structures and varied during the all-atom optimizations for **1I** structure variants. The total energy of systems **2A** and **2B** was determined using the same methodology as described above. The **2B** model without *n*-heptane was additionally reoptimized allowing all-atom positions to vary. During all calculations, the Monkhorst–Pack grid[48] was used to sample the Brillouin zone. The NMR chemical shifts were computed using the GIPAW (gauge including projector augmented waves) method. When calculating the full crystal structure, a plane wave basis set with a maximum cutoff energy of 570 eV was used. Finally, we obtained NMR chemical-shielding values in periodic boundary conditions using the fully optimized structure. In all cases, the optimization algorithm was BFSG[49] with line search.

Calculation of Free Volume Space. The void volumes were calculated using Mercury CSD 3.9 software[50] with a probe radius of 0.5 Å and a grid spacing of 0.3 Å applied for the contact surface.

RESULTS AND DISCUSSION

(i) Analysis of Desolvation Process by Means of Solid State NMR Spectroscopy. The migration process of guest molecules from the crystal lattice of sample **1** was investigated in a previous project by García-Garibay et al.[26] Employing X-ray powder diffraction (PXRD) analysis, it has been proven that release of acetonitrile from the lattice causes reorganization of the structure. In consequence, two crystal forms of **1** exist, both with $P2_1$ symmetry and $Z' = 1$. The first one, labeled as **1A** contains two solvent molecules in the unit cell. The second one, called **1B**, is a solvent free form. During the releasing of guest molecules, the host units undergo rearrangement and the size of the unit cell is changed. For **1A,** the volume is about 15% larger than for **1B**. This process is shown in Scheme 1 in pictorial form. The PXRD data clearly proved that the pathway from **1A** to **1B** is a three-step process with formation of an intermediate product which we labeled as **1I**. The crystal structures of both **1A** and **1B** were established by means of single crystal X-ray diffraction studies (sc XRD). The structure of **1I** has not been reported to date.

In the course of our studies we have found that the process of migration of solvent molecules can be recognized by solid state NMR. Figure 2 shows the ^{13}C CP/MAS spectra of a freshly crystallized sample **1A** (Figure 2A). It has to be stressed that this form is highly unstable. Successful measurement was carried out in a special closed insert placed in 4 mm zirconium rotor. Sample **1A** kept in an opened vessel at ambient temperature gradually loose the solvent occluded in the crystal lattice and is converted to quasi-stable sample **1I** (Figure 2B).

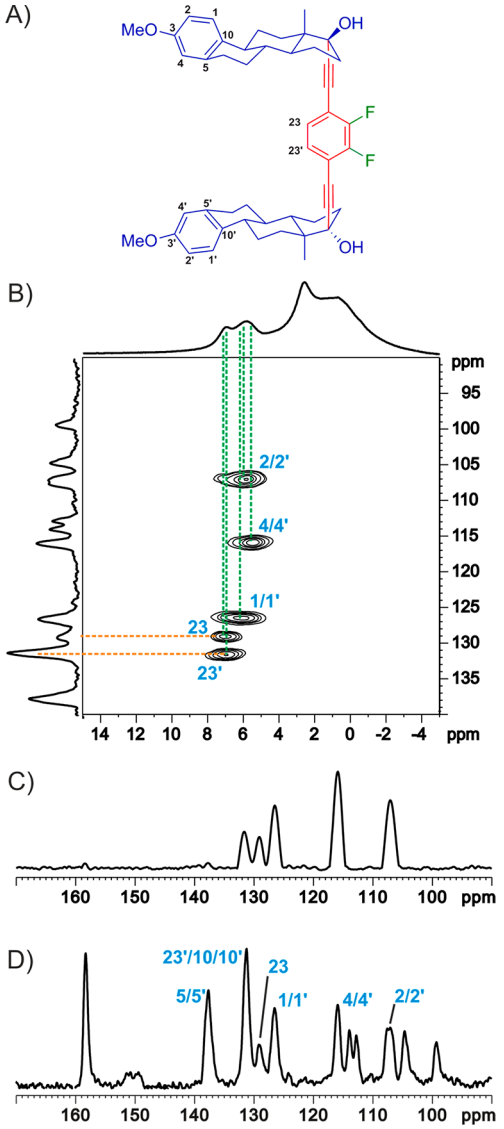

Figure 3. Molecular structures of **1** with numbering system adapted from ref 26 (A). The $^{1}H-^{13}C$ inv-HETCOR NMR spectra for **1B** (B) and their projection along F2 dimension (C) recorded with 150 μs second contact time as well as ^{13}C CP MAS NMR spectra (D). All data were acquired at a 42 kHz spinning rate at ambient temperature.

The further thermal treatment of **1I** at 165 °C leads to the solvent free, stable structure **1B** (Figure 2C). Nevertheless slow conversion **1I** to **1B** form is observed also during the NMR measurements (performed at ambient temperature without cooling of sample). The distinction between forms of **1** is recognized by ^{19}F MAS measurements (Figure 2D–F). Forms differ in ^{19}F chemical shifts and number of isotropic signals (double peaks for **1I**).

From the inspection of ^{13}C CP/MAS spectra it is apparent that each sample presents different pattern. The most diagnostic ^{13}C resonances related with desolvation process is the region close to 0 ppm. This signal corresponds to the methyl residues of acetonitrile (indicated by green ellipsoid in Figure 2). As seen the intensity of the acetonitrile signal is ca. two times lower for **1I** compared to **1A**, and it is completely undetectable for **1B**. Next a striking difference between all forms is the larger number of ^{13}C resonances for **1I** both in aromatic and aliphatic regions compared to **1A** and **1B**.

https://dx.doi.org/10.1021/acs.cgd.9b01179
Cryst. Growth Des. 2020, 20, 2202–2216

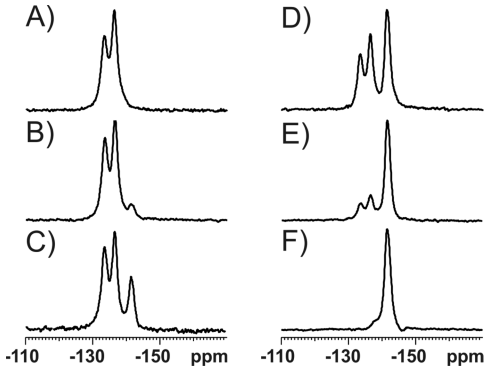

Figure 4. ^{19}F MAS NMR spectra of **1I** recorded with cooling of sample at 5 °C. (A) Immediately after crystallization and after (B) 5 min, (C) 15 min, (D) 2 h, and (E) 18 h spun in magnet at ambient temperature (approximately 55 °C inside the rotor). (F) Spectrum of sample **1I** after heating at 165 °C. All spectra were recorded with a spinning rate of 25 kHz.

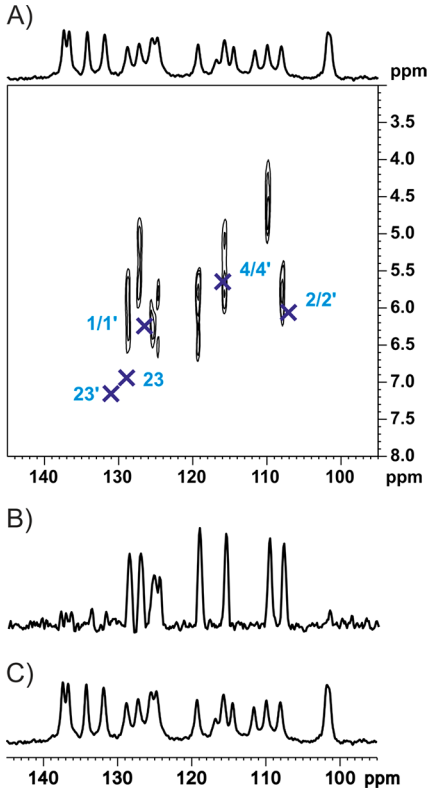

Figure 5. ^{13}C-^{1}H-FLSG HETCOR NMR spectra for **1I** (A) and their projection along the F2 dimension (B) recorded with 150 μs contact time as well as ^{13}C CP MAS NMR spectra (C). All spectra were acquired at a 13 kHz spinning rate at 5 °C. The HETCOR spectra also indicate (blue crosses) the correlations and assignments obtained for **1B** sample.

From single crystal XRD studies of **1A** and **1B**, we know the Z' values for both samples ($Z' = 1$). According to basic NMR knowledge for such systems in ^{13}C spectra, we should observe the number of resonances which truly reflect molecular structure. Obviously this is not the case for **1A** and **1B**. Very likely for these compounds crystallographically nonequivalent positions are magnetically equivalent making the assignment of ^{13}C signal ambiguous. These unexpected difficulties in structure analysis prompted us for application of advanced solid-state NMR techniques. In the first approach we have employed a methodology based on very fast magic angle spinning (VF MAS) with sample rotation above 40 kHz. This technique, which requires small size NMR rotors (1.3 mm diameter) has found a spectacular number of applications in structural analysis of natural products and synthetic compounds.[S1,S2]

Our study began with the most stable, solvent-free form **1B**. In order to assign ^{13}C and ^{1}H resonances in one experiment we applied 2D NMR measurements. Application of the VF MAS technique opens a way to significantly increase sensitivity for heteronuclear correlation experiments by the application of inverse ^{1}H-detected technique (inv-HETCOR) that became available with a very high spin rate of the sample. This experiment gives well-separated ^{1}H−^{13}C correlations allowed to assign ^{1}H chemical shifts, very sensitive to structural changes and further straightforward assignment of ^{13}C signals belonging to aromatic rotator residue. Figure 3 shows the aromatic region of inv-HETCOR for sample **1B** recorded with a spinning rate 42 kHz. The full spectrum is attached as SI. To be consistent with previously reported data we adopted a numbering system reported elsewhere (Figure 3A).[26] Through analysis of the spectrum (Figure 3B) and their F1 projection (Figure 3C), we assigned five well separated aromatic signals which correspond to the protonated positions of carbons. Therefore, all other signals in this region (Figure 3D) should be assigned to the aromatic quaternary carbon positions. Our assignment was supported by GIPAW calculations (see the discussion in section ii). Presented results permit us to conclude that C−H positions for 23 and 23′ carbons are not magnetically equivalent. Moreover, the signal from carbon 23′ overlaps with quaternary 10/10′ positions and thus explains the high intensity of signal at ca. 131 ppm in ^{13}C CP/MAS experiment.

Unfortunately, attempts to apply a similar VF MAS approach for analysis of **1I** totally failed. One of the major problems occurring for this sample is its instability above room temperature. The heating of the rotor through friction air during such extremely high spinning can increase the ambient temperature even by 40−60 °C. The centrifuge power can be an additional factor accelerating transition. Thus, despite several attempts, we were not able to carry out measurements for **1I** employing VF MAS techniques. Even application of cooling during NMR measurements (−20 °C, which was the lowest temperature possible to reach by our probehead) was not sufficient to prevent transition of **1I** to form **1B**.

Thus, going further with our NMR studies of **1I** we employed a 2.5 mm rotor which allows sample spinning with lower speed up to 25 kHz. However, even at such a moderate spinning rate, despite the temperature stabilization at 5 °C, the phase transition is observed. The ^{19}F MAS spectra shown in Figure 4 provides evidence confirming spun modulated phase transition in magnet. The process of change of **1I** to **1B** is slow enough to be detected *in situ* by the recording of a series of Bloch decay (BD) ^{19}F MAS NMR spectra (Figure 4). The intensity of signals in BD experiments is proportional to the number of magnetically equivalent spins in the sample, and thus it is possible to quantitatively answer at any point of the desolvation process what is the ratio between form **1I** and **1B**. This is an advantage of direct detection over the cross-polarization type experiment which does not provide quantitative information.

https://dx.doi.org/10.1021/acs.cgd.9b01179
Cryst. Growth Des. 2020, 20, 2202−2216

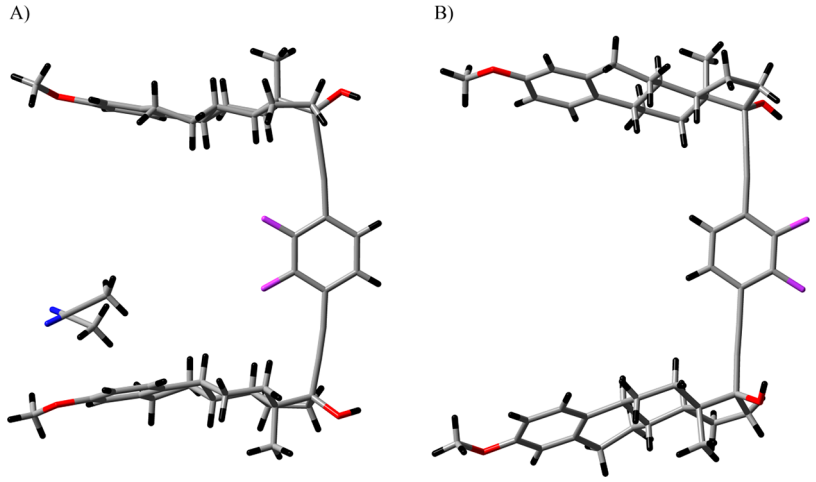

Figure 6. Molecular structure of (A) **1A** and (B) **1B** in the crystal lattice.

Table 1. Experimental and Calculated Results of ^{1}H Chemical Shifts [ppm] for Position 23/23′ in Structure 1A, 1I, and 1B[a]

experimental	1A	1I	1B
	ca. 5.5[b]	ca. 5.8[b]	6.9/7.2
calculated	1A	1A (without CH_3CN)	1B
X-ray	5.4/5.5	5.6/5.8	7.1
rotated up to ±90°	5.6−5.8	5.6−5.9	7.1−7.4

[a]Calculated results are presented for various orientations of the rotator part of the molecule, and they are recalculated from nuclear shielding using equation presented on Figure S5. [b]Assignment of signal made according to comparison results for **1I** and **1B** forms.

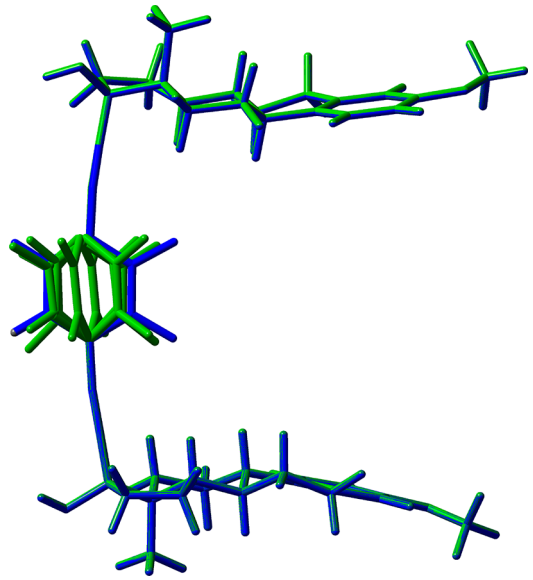

Figure 7. X-ray structure (blue) and examples of constructed models (green) with various orientations of the rotator part of the molecule for **1A**.

Keeping in mind that even a 25 kHz spinning speed is dangerous for sample **1I** we slowed down the spinning rate to 13 kHz. Under such conditions, the cooling system for a 2.5 mm probehead is very effective and sample **1I** is protected and stable. The 1D ^{13}C CP/MAS spectrum suggests that in the case of **1I** each crystallographically nonequivalent position is also magnetically nonequivalent thus explaining the larger number of resonances compared to **1A** and **1B**. Under a low spinning rate, in order to obtain high quality 2D NMR HETCOR correlations with direct detection of ^{13}C nuclei, an approach employing FSLG ^{1}H decoupling[53] has to be applied to guarantee the high resolution in the F1 domain. The aromatic region of 2D correlation recorded for **1I** is shown in Figure 5. The short contact time of 150 μs was set up to observe only correlations of carbons directly bonded to protons. In this approach, the quaternary and protonated ^{13}C signals can be distinguished by comparison projection of the F2 dimension of HETCOR experiments with the ^{13}C CP MAS spectrum (Figure 5B−C). In Figure 5A we added also the positions of "cross-peaks" recorded for **1B** at VF MAS regime (blue crosses). From this comparative analysis, it is apparent that the biggest changes of chemicals shifts during the transformation are manifested by ^{1}H resonances. The high sensitivity of proton solid state NMR to even small structural modifications is well-known and was discussed in our previous papers and by other authors.[54−58]

Finally, we carried out 2D FSLG HETCOR correlation for **1A**, the most demanding sample from the NMR point of view. We assigned the position of aromatic signals and ^{1}H, ^{13}C chemical shifts for quaternary and C−H carbons. The spectrum is attached as SI (Figure S4). As revealed, the proton chemical shifts for the aromatic ring of the rotator are in the region found for sample **1I**.

(ii) Mechanism of Phase Transition for 1—GIPAW Calculations. Inspection of the X-ray structure of **1** clearly shows that during the desolvation process, the fluorinated rotator of sample **1A** undergoes a ∼180° jump. This phenomenon is shown in pictorial form in Figure 6. The challenging questions related with this process regard the timing of the jump and further whether this turn is correlated with phase transition or is independent. The answer to this question whether it occurs on the first stage between **1A** and **1I** or during the second transformation between **1I** and **1B** is not trivial because as we highlighted *supra* single crystal X-ray data for **1I** are not available. To discuss the hypothetical mechanism of transformation we used a set of NMR parameters for **1** reported in section i and a quantum chemical method which allows joining both approaches in one platform.

Today the most powerful and commonly used quantum chemical routine for computing solid state NMR parameters is

https://dx.doi.org/10.1021/acs.cgd.9b01179
Cryst. Growth Des. 2020, 20, 2202−2216

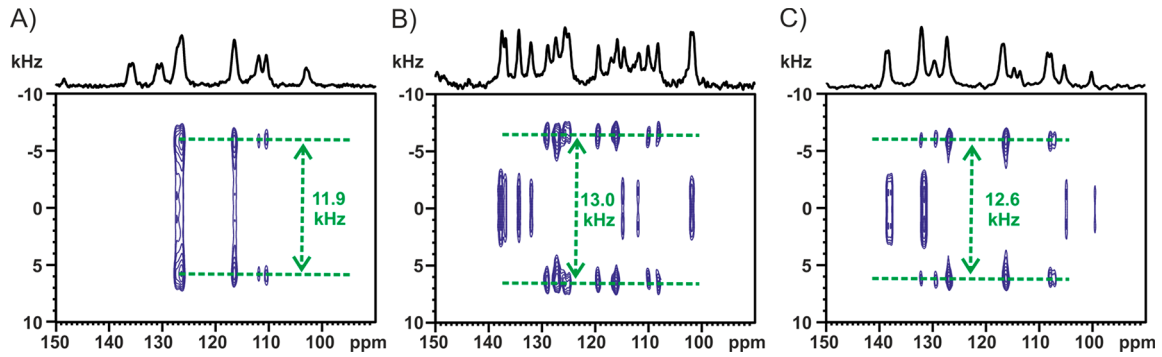

Figure 8. 2D PISEMA MAS spectra for sample **1A** (A), **1I** (B), and **1B** (C) in the aromatic region. The highest splitting values are labeled in each spectrum. All spectra were acquired at a 13 kHz spinning rate.

Table 2. Experimental Results of ^{13}C Chemical Shift Tensors [ppm] for 23/23′ Positions of Structure 1A and 1B

structure	δ_{iso}	δ_{11}	δ_{22}	δ_{33}	Ω^a
1A	130.7	242.8	96.0	53.5	189.3
1B	131.3	239.3	105.8	48.9	190.4

[a]Span is expressed as $\Omega = \delta_{11} - \delta_{33}$.

Table 3. Calculated ^{13}C NMR Chemical Shift Tensors [ppm] for 23/23′ Positions of Structure 1A and 1B Calculated Using the PBE Functional with Ultrasoft Pseudopotential and the GIPAW Approach[a]

structure	δ_{iso}	δ_{11}	δ_{22}	δ_{33}	Ω^b
1A	126.4	217.9	144.5	16.9	201.0
	127.5	217.9	150.8	13.7	204.2
1B	130.5	219.5	150.1	22.1	197.4
	134.1	222.9	154.2	25.2	197.7

[a]Data are obtained after recalculation of nuclear shieldings according to the equation from Figure S5. [b]Span is expressed as $\Omega = \delta_{11} - \delta_{33}$.

the GIPAW methodology[44,45] introduced by Pickard and co-workers. It takes into consideration the periodic crystal structure rather than an isolated molecule. Such a technique allows a combination of theoretical and experimental approaches to be used by comparison of calculated NMR shielding parameters with experimental chemical shifts. It creates a complementary approach which is able to precisely analyze very subtle structural effects.

As in the case of section i our calculation began with sample **1B**. The single crystal X-ray data (refcode TIWYAB) were taken as an input file. A full set of computed ^1H and ^{13}C shielding parameters and their correlations to the experimental results are given as Supporting Information.

The same approach was applied for sample **1A**. The single crystal X-ray data (refcode TIWXUU) was applied for further GIPAW calculations. It has to be expressed that computed shielding parameters of most diagnostic positions represented by proton chemical shifts for 23/23′ residues (rotator signals) very well follow the experimental data. Table 1 collect all obtained ^1H chemical shifts for 23/23′ position for the studied models and theoretical NMR parameters.

Going further with our calculations we constructed and optimized (using GIPAW methodology) virtual systems employing as starting models true X-ray structures. First, we were prompted to answer the question concerning the influence of two solvent molecules in the crystal lattice of **1A** on proton chemical shifts for 23/23′ C−H positions. We

Table 4. Crystal Structure and Refinement Data

compound	**2A**	**2Ar**	**2B**
empirical formula	$C_{72}H_{96}F_2O_{10}$	$C_{72}H_{96}F_2O_{10}$	$C_{79}H_{112}F_2O_{10}$
formula weight	1159.49	1159.49	1259.69
temperature	100 K	293 K	173 K
crystal system	triclinic	triclinic	monoclinic
space group	P1	P1	$P2_1$
a (Å)	7.5267(3)	7.5896(3)	6.9762(2)
b (Å)	10.9638(4)	10.9648(7)	34.1404(11)
c (Å)	20.6904(9)	21.1603(13)	16.1012(5)
α (deg)	101.950(3)	103.671(15)	90
β (deg)	99.218(4)	98.127(4)	92.624(2)
γ (deg)	90.228(3)	90.076(4)	90
volume $(Å)^3$	1647.61(12)	1692.75(17)	3830.8(2)
Z	1	1	2
density $(g{\cdot}cm^{-3})$	1.169	1.169	1.092
θ range (deg)	4.12 to 75.72	4.11 to 74.87	2.19 to 27.48
index ranges	$-9 \le h \le 9, -13 \le k \le 13, -25 \le l \le 25$	$-9 \le h \le 5, -13 \le k \le 13, -24 \le l \le 26$	$-7 \le h \le 9, -43 \le k \le 42, -20 \le l \le 18$
Nref	11847	8126	17254
R (reflections)	0.0986 (10623)	0.0924 (6804)	0.0593 (8781)
wR_2 (reflections)	0.2701 (11847)	0.2758 (8126)	0.1624 (13506)

removed separately one of them and finally both. Our calculations proved that the influence of acetonitrile on chemical shifts of 23/23′ protons is negligible. Second, we built models with different orientations of rotator ring versus steroidal residue for **1A** and **1B**. This idea in pictorial form is shown in Figure 7. Most of the models were found the be unstable and during optimization flip back to the starting **1A** or **1B** native conformations was observed. In local energy minimum ^1H theoretical chemical shifts were found to be very similar to experimental data measured for native samples. It is important to express that all generated models for both **1A** and **1B** crystal structures have global energy higher than the structure with native conformation meaning that the preferred conformations are those presented in the crystal structures.

Concluding, our calculations suggest that the distinction of ^1H chemical shifts for C23/C23′ residues in **1A**, **1I**, and **1B** is related to local environmental effects strengthened by crystallographic effects (molecular packing, size of the unit cell). Thus, comparing the ^1H chemical shifts we can assume

https://dx.doi.org/10.1021/acs.cgd.9b01179
Cryst. Growth Des. 2020, 20, 2202−2216

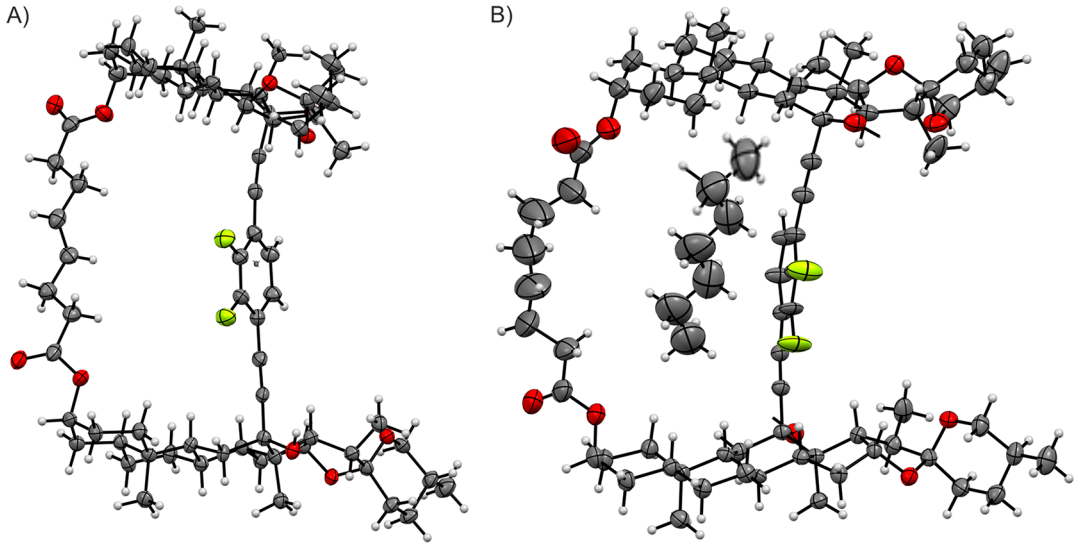

Figure 9. Molecular structure of (A) **2A** and (B) **2B** with the thermal ellipsoids drawn at 50% probability for every atom other than hydrogen.

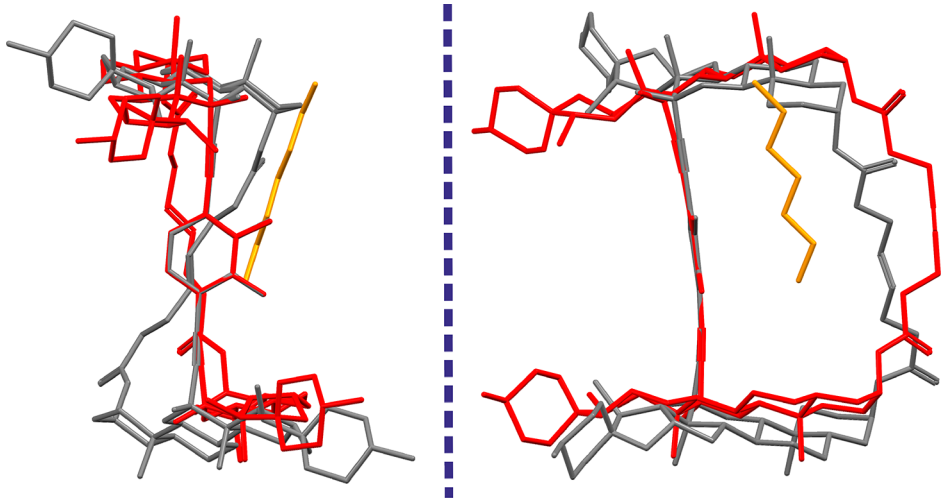

Figure 10. Superposition of **2A** (gray) and **2B** (red). The *n*-heptane molecule is colored orange. The phenyl rotators are placed overlaid.

Scheme 2. Unit Cell Thermal Transformation 2B → 2A

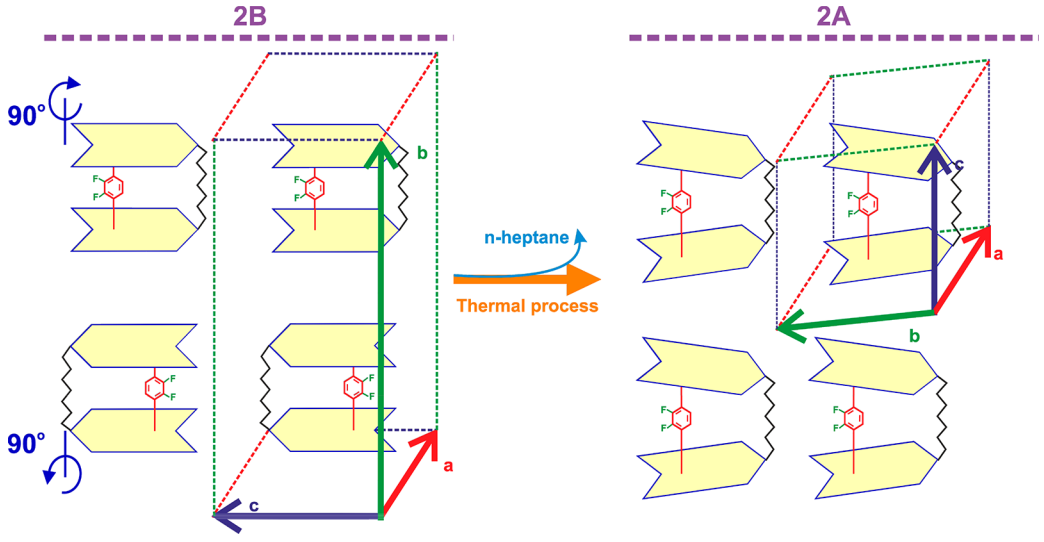

https://dx.doi.org/10.1021/acs.cgd.9b01179
Cryst. Growth Des. 2020, 20, 2202−2216

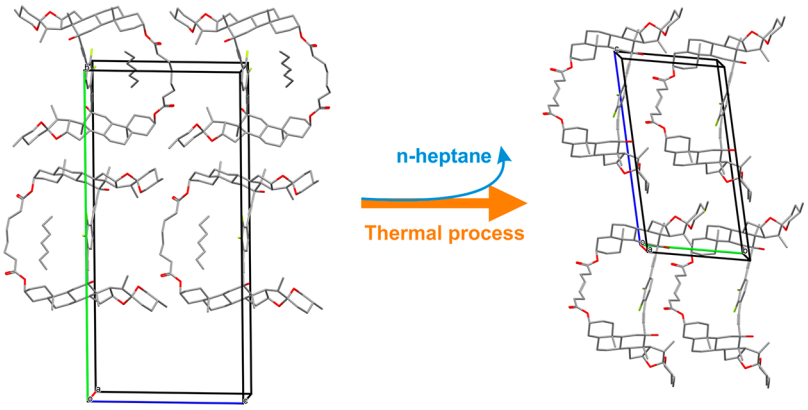

Figure 11. Crystal packing of **2B** (left) and **2A** (right).

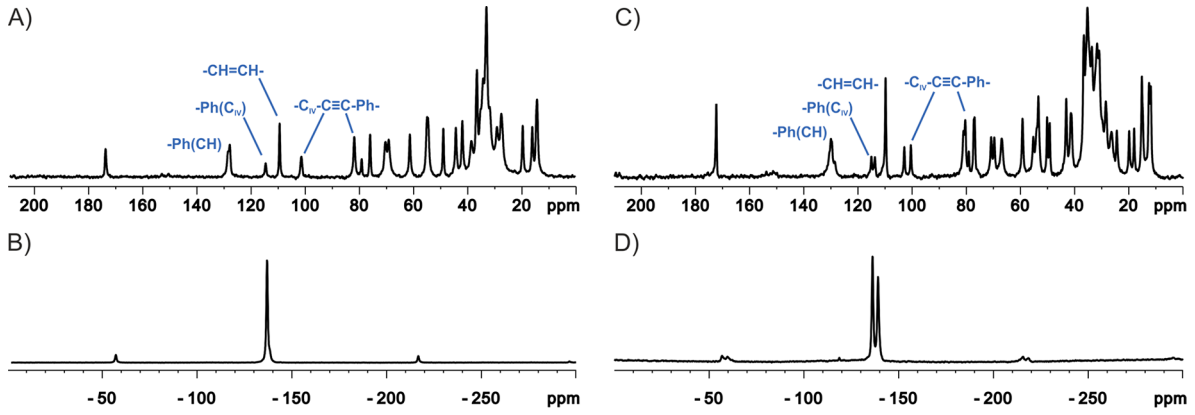

Figure 12. $^{1}H \rightarrow {}^{13}C$ CP MAS (A, C) and ^{19}F MAS NMR (B, D) spectra of **2A** (A, B) and **2B** (C, D) recorded at ambient temperature with a spinning rate of 10 kHz (A, C) and 30 kHz (B, D).

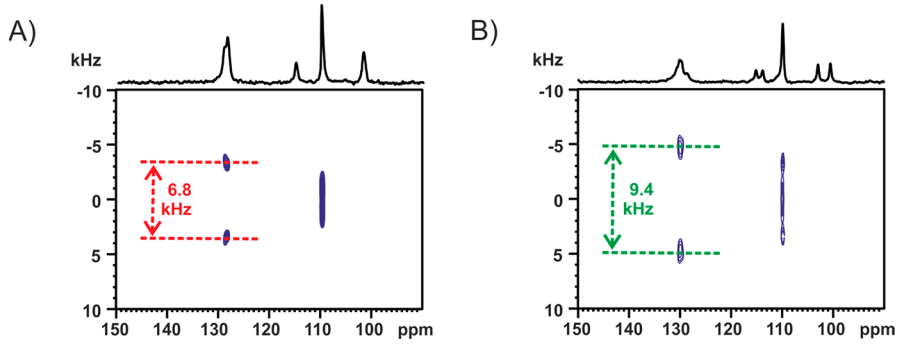

Figure 13. 2D PISEMA MAS spectra for sample **2A** (A) and **2B** (B) in the aromatic region recorded at ambient temperature with a spinning rate of 13 kHz.

Table 5. Experimental Results of ^{13}C Chemical Shift Tensors [ppm] for 23/23′ Positions of Structures 2A and 2B

structure	δ_{iso}	δ_{11}	δ_{22}	δ_{33}	Ω^{a}
2A	127.4	178.1	128.8	75.6	102.5
2B	129.2	189.1	134.8	63.7	125.3

[a]Span is expressed as $\Omega = \delta_{11} - \delta_{33}$.

that **1I** in terms of orientation of the rotator with respect to the steroidal framework, is structurally closer to **1A** than to **1B**. Very likely the jump of fluorinated phenyl ring takes place during **1I** → **1B** transformation and is synchronized with change of the size of the unit cell.

Table 6. Calculated ^{13}C NMR Chemical Shift Tensors [ppm] for 23/23′ Positions of Structures 2A and 2B Calculated Using the PBE Functional with Ultrasoft Pseudopotential and the GIPAW Approach[a]

structure	δ_{iso}	δ_{11}	δ_{22}	δ_{33}	Ω^{b}
2A	129.1	217.9	142.3	26.9	191.0
	129.9	219.8	147.7	22.3	197.5
2B	132.3	222.4	152.1	22.5	199.9
	128.0	217.3	146.9	19.7	197.6

[a]Data are obtained after recalculation of nuclear shieldings according to the equation from Figure S5. [b]Span is expressed as $\Omega = \delta_{11} - \delta_{33}$.

https://dx.doi.org/10.1021/acs.cgd.9b01179
Cryst. Growth Des. 2020, 20, 2202−2216

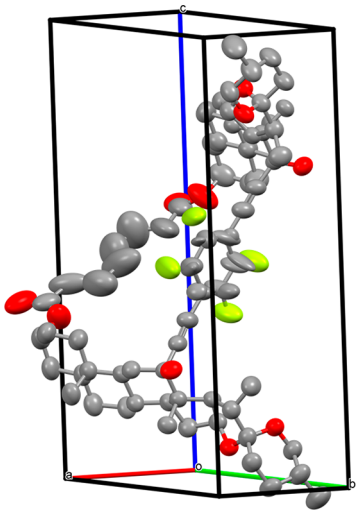

Figure 14. Room temperature single crystal X-ray unit cell of **2A** with the thermal ellipsoids drawn at 50% probability for every atom other than hydrogen.

(iii) Study of Local Molecular Motion for 1 Employing $^{1}H-^{13}C$ Dipolar Coupling Analysis and ^{13}C Chemical Shift Anisotropy. Results presented in sections i and ii rather exclude the opportunity of free rotation of aromatic ring around the 1−4 axis for samples under investigation. It is worthy to recall that such process is common for unsubstituted rotator residues in other steroidal systems published elsewhere.[59,60] It has to be stressed that the above-mentioned data for **1** do not eliminate possibilities of small amplitude motions: wobbling, local vibrations. In our previous paper, studying the local molecular motion in the crystal lattice of aromatic residues in the steroidal rotators we have tested applicability of solid state NMR techniques based on the analysis of $^{1}H-^{13}C$ dipolar couplings and change of ^{13}C chemical shift anisotropy (CSA).[29] Both techniques are suitable for inspection of motion in the kHz time scale (below $10^{-3}-10^{-6}$ s).[61,62]

In the first approach we have used a methodology based on analysis of C−H dipolar interactions.[63] The splitting between the singularities of the C−H doublet reflects the dipolar coupling between the proton and carbon. According to the equation $d = -[\mu_0/(4\pi^2)](\gamma_i\gamma_j)/r_{ij}^3$, the dipolar coupling constant for the rigid limit for a $^{1}H-^{13}C$ distance equal to 1.09 Å is 22.7 kHz. The experimentally measured d_{expt} values are smaller than the calculated coupling because splitting is reduced by a scaling factor.[64] The experimental d_{expt} is equal to $\cos(\vartheta_m) \times d$ where ϑ_m is the magic angle (54.7°) giving a scaling factor of 0.577. In the rigid system, the expected splitting value is approximately 13.1 kHz (0.577 × 22.7 kHz). Molecular motion can reduce the values of principal components of the dipolar tensor diminishing d_{expt} up to 6.5 kHz as the minimum value.

In our work, for measurements of C−H dipolar coupling we have employed 2D PISEMA MAS sequence. Figure 8 shows spectra recorded in 2D mode for samples **1A**, **1I**, and **1B**. From the inspection of data it is apparent that d_{expt} splittings for **1A**, **1I**, and **1B** are large but slightly different with the smallest value for **1A** (d_{expt} = 11.9 kHz). As predicted, these results exclude rotation of the aromatic rotator around the 1−4 axis in each case. We can only speculate the small amplitude wobbling of the rotator for sample **1A**. According to our previous experience free jumps around the 1−4 axis should reduce d_{expt} to ca. 7 kHz.[29]

Going further with investigation of dynamic processes in different forms of sample **1** in the next step, we examined ^{13}C CSA. CSA parameters can be obtained from line-shape analysis employing spinning side-bands pattern. Such a pattern is recorded by reducing the spinning rate of the sample and adjusting it to immanent features of the nuclei under investigation. Low spinning 1D principal component measurements can be only used with relatively simply spectra as ^{19}F MAS. Figure S6 shows the ^{19}F MAS spectra recorded with a spinning rate of 30 kHz and 10 kHz. The calculated principal components of the chemical shift tensor ^{19}F δ_{ii} are collected in Table S1.

For the ^{13}C nuclei due to higher overlapping of signals, sensitivity issues as well as much more complicated spectra compared to ^{19}F similar to the above approach cannot be applied. This drives the need for 2D NMR techniques. There are several techniques that allow the separation of the isotropic and anisotropic portions of the spectra for heavily overlapped systems.[65,66] In this work, we employed the 2D PASS sequence for analysis of ^{13}C spectra which offers good sensitivity compared to other methods.[67] The numerical data for 23/23′ positions of **1A** and **1B** are collected in Table 2.

The criterion which is a measure of dynamic processes followed by CSA analysis is the comparison of experimental values with computed parameters.[68] In standard GIPAW procedure, the results are recalculated to chemical shifts using the equation: $\delta_{ii}^{calc} = \sigma_{ref}^{calc} - \sigma_{ii}^{calc}$ where σ_{ref}^{calc} value is obtained by calculating the chemical shift of an external reference sample or, as it was done in our work, may be determined by linear regression of a plot for experimental shifts against calculated shielding (Table 3).

Comparative analysis of experimental and theoretical ^{13}C δ_{ii} NMR data reveals that aromatic residues in **1A** and **1B** forms are rather rigid. For comparison we have taken Ω_{theo} and Ω_{expt} values. For **1A** parameter Δ expressed by equation $\Delta = \Omega_{theo} - \Omega_{expt}$ is around 12 ppm while for **1B** Δ is ca. 7 ppm. In our previous works we proved that lack of such consistency (above ca. 50 ppm) is a measure of dynamics processes.[68] It is worth to note that any of the experimentally obtained Ω values for aromatic signals is around 200 ppm. The conclusion coming from analysis of ^{13}C CSA data is consistent with PISEMA MAS measurements. The values of dipolar $^{1}H-^{13}C$ splitting do not support the suggestion that rotator undergoes large amplitude reorientation in time range $10^{-3}-10^{-6}$s.

In the case of computing fluorine NMR shielding parameters, the problem is more complex. This issue was recently discussed by Dybowski and co-workers.[69] In the cited paper, the authors highlighted that conventional computational approaches based on density-functional theory (DFT) are often incapable of quantitative prediction of ^{19}F magnetic shielding. Hence, we did not confront ^{19}F experimental with theoretical results for discussing dynamic process. Fortunately, ^{13}C NMR CSA measurements do not suffer from that issue as was proved elsewhere.[68]

(iv) X-ray Structure Analysis of Sample 2. In order to keep consistency between the structural studies for sample **1** and **2** in the first approach we followed the crystallization procedure described in ref 26 for obtaining crystals of **2** employing the CH_3CN solution. The X-ray analysis for this sample revealed the absence of solvent within the asymmetric unit. We labeled this form as **2A** and for room temperature

https://dx.doi.org/10.1021/acs.cgd.9b01179
Cryst. Growth Des. 2020, 20, 2202−2216

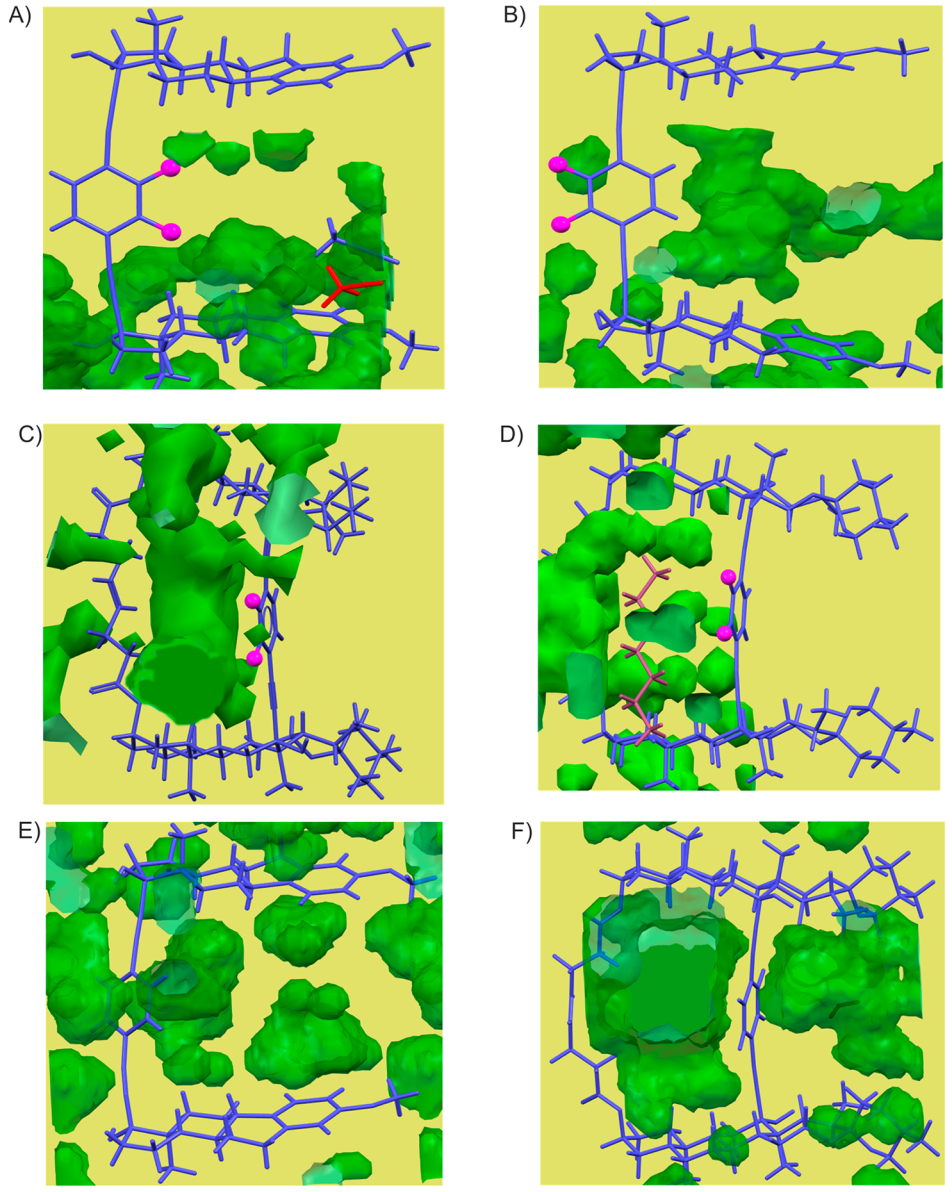

Figure 15. Visualization of the voids (empty space) volumes in the crystal lattices of (A) **1A**, (B) **1B**, (C) **2A**, (D) **2B**, (E) **1-H**, and (F) **2-H** using probe radius 0.5 Å calculated using the contact surface. The voids are colored by green whereas the yellow color represents space not accessible with that condition.

structure **2Ar.** In the next step we obtained the crystalline material from CH_2Cl_2 and *n*-heptane solution. This form is called **2B**. X-ray data for this sample clearly showed the presence of *n*-heptane inside the cavity formed between the phenylene rotator and the polymethylenic bridge (presence of *n*-heptane in bulk material was also proved by liquid state NMR (Figure S7, Supporting Information)). The crystallographic data for **2A**, **2Ar**, and **2B** are collected in Table 4 and Figure 9.

Single crystal X-ray diffraction (sc XRD) studies proved that compound **2A** crystallizes in the triclinic *P*1 space group with one molecule per unit cell while **2B** crystallizes as a heptane solvate in the monoclinic $P2_1$ space group with two molecules per unit cell and $Z' = 1$. As depicted in Figure 9, the steroidal stators acquired a *syn* conformation with respect to each other. The absolute configuration of the vinylene fragment could also be unambiguously assigned to the *E* isomer. Moreover, it can be seen that both steroidal backbones are aligned with their *α*-faces oriented toward the C_2 symmetry axis perpendicular to the rotational 1,4-diethynylphenylene axis. A comparison of the asymmetric units of **2A** and **2B** is presented in Figure 10. It can be seen that in the case of **2A** a wider torsion of 60° between both rotators is observed in contrast to 10° for the solvate form **2B**. Nonetheless, at the molecular level the symmetry is preserved upon thermal treatment, as the quasi C2 symmetry axis perpendicular to the rotator prevails in both structures. Although both structures feature noncentrosymmetric self-assemblies and intralayer weak C−H···F interactions among adjacent rotators as the fundamental supramolecular motif, an important crystallographic difference between both structures arises from the existence of a clear interlayer screw axis in **2B** spreading along the crystallographic *b* axis, which is absent in the solvent-less form **2A**. The room temperature structure **2Ar** clearly shows disorder in the rotor part (difluorophenyl ring), and two alternative positions of it could be determined with relative occupancy ratios of 0.59−

https://dx.doi.org/10.1021/acs.cgd.9b01179
Cryst. Growth Des. 2020, 20, 2202−2216

0.41 and almost planar orientation of two conformers with a dihedral angle between them of 171°. The hexylene linkage fragment (with vinylene central part) possesses much higher thermal displacement parameters in **2Ar** structure in comparison to **2A**. The thermal displacement parameters of this fragment in **2Ar** are probably a combination of two main factors: higher thermal vibration of atoms at room temperature and multiple conformations similar enough that cannot be modeled as two or three alternative positions. It may be possible that rotation of the difluorophenyl ring in **2Ar** requires some mobility of the hexylene linkage and this is visible in the structure which reflects a cooperative dynamic between both connective fragments joining spiro-3-ol moieties.

The halogen interaction C−H···F stabilizes the crystal packing of **2A**; there is a continuous chain of these hydrogen bonds running along the *a* direction (001) of the crystal lattice. The rotation of the difluorophenyl ring in the **2Ar** structure does not prevent their formation, and the second orientation creates them as well; however, if the neighboring cells possess an alternative conformation of the rotors, then the negative interaction F···F is present. The restriction of rotation in fluorine substituted phenyls may have this as one of the contributing factors.

(v) Mechanism of Phase Transition for 2. In section ii we discussed the mechanism of thermal phase transition for sample **1** synchronized with solvent migration from the crystal lattice. In the case of **1**, the crystal system and space group were preserved. Storing sample **2B** at 130 °C for 30 min we observed an unusual process, reorganization of crystal structure **2B** to form **2A** and dramatic change of the crystal system and space group. The mechanism of thermal transformation **2B** → **2A** is shown in Scheme 2 and Figure 11. The loss of *n*-heptane solvent modifies the hydrophobic short contacts observed in **2B** structure and replaces them by the intermolecular hydrogen bonds between carboxyl groups (**2A**). Such chemical modification influences the crystal packing which undergoes significant change by rotating molecules in every second layer by approximately 90° in one direction and in every other layer in the opposite direction by the same 90° angle causing a half shortening of the *b* crystallographic axis (and become a "new" *c* axis) and removal of the 2-fold screw axis. Additionally, the molecule itself shows a characteristic "twist" as was shown in Figure 10. These factors cause reduction of crystal symmetry to *P*1 (starting from $P2_1$). Such scheme explains in detail the mechanism of **2B** → **2A** thermal transformation. The dynamic effects in molecular crystals is actually one of the most challenging subjects.

The apparent question which is crucial for more deeply understanding the mechanism of transformation is related with the driving force for this process. Such large amplitude motion as described above, a jump of the whole molecule in the crystal lattice, requires adequate energy. Thus, we assumed that form **2B** is thermodynamically not favored. In order to verify this hypothesis we computed the energy of crystals both for **2A** (Z = 1) and **2B** (Z = 2). The GIPAW calculations for **2A** gave a value of −18 621.692 eV (−1 796 714.0 kJ) while for **2B** (after removing of *n*-heptane) the value is found −37 241.612 eV (−3 593 256.9 kJ). The calculated data proved the significant energetic preference for the **2A** structure. The difference between both structures can be recalculated to value 86.0 kJ/mol per one molecule.

(iv) ^{1}H, ^{13}C, ^{19}F Solid State NMR Study of Structure, Dynamics, and Thermal Stability of 2. Figure 12 shows ^{13}C and ^{19}F solid state NMR spectra of **2** recorded at ambient temperature employing the magic angle spinning techniques. In the first approach, the ^{1}H → ^{13}C CP MAS experiments for freshly crystallized samples **2A** and **2B** were carried out. The recorded sharp signals are straightforward evidence confirming the high crystallinity of the samples. Figure 12 displays also the ^{19}F MAS NMR spectra recorded with spinning rate 30 kHz. As one can see in this case we observed only one signal in the isotropic part for **2A** and two well resolved resonances for **2B**. Therefore it is apparent from inspection of the spectrum that both fluorine positions for **2B** are crystallographically and magnetically nonequivalent whereas it is not the case for **2A** where two crystallographically different positions lead to one ^{19}F isotropic signal.

For inspection of dynamics processes of **2A** and **2B** we have used similar NMR tools as in the case of sample **1**. Figure 13 shows ^{1}H−^{13}C PISEMA MAS experiment for **2A** and **2B**. The values of the ^{1}H−^{13}C dipolar splitting are significantly lower compared to values found for sample **1**. In particular the value of splitting for **2A** (6.8 kHz) is spectacular. In our papers published elsewhere we have proven that such a value reflects the fast molecular motion of aromatic residues.[70,71]

We have also established ^{13}C δ_{ii} parameters employing methodology (2D PASS) applied previously for the study of sample **1**. Additionally, advanced theoretical calculations using GIPAW approach were employed to analyze ^{13}C σ_{ii} shielding parameters. The results of quantum mechanical calculations for ^{13}C of −Ph(CH) positions and experimental values of chemical shifts are shown in Tables 5 and 6. For **2A** the Δ parameter is ca. 95 ppm. The values of dipolar ^{1}H−^{13}C dipolar splitting and ^{13}C CSA parameters give a consistent picture confirming the free rotation of the aromatic residue around 1−4 axis.[68] For **2B** we can only speculate low amplitude wobbling for fluorinated derivatives (the Δ parameter is around 70 ppm).

The dynamic process of the rotator was additionally proved by the room temperature single X-ray measurements. Figure 14 clearly shows two possible positions (case of uncertainty) of the fluorine atoms oriented in the opposite side of phenyl ring. The occupancy ratio 59:41 justify that the applied solid state NMR methodology provides high accuracy data which with no doubts describes the dynamic process.

(vii) Free Volume Surface Analysis for 1, 2, and Their H-Analogs. In the Introduction, we highlighted that one of the prerequisites, which has to be fulfilled in the case of molecular rotors, is appropriate space for reorientation of the mobile fragment (rotator) in the system under consideration. The void volume can be estimated by analysis of X-ray data using contact surface maps with probe radius 0.5 Å calculated using the contact surface where the volume can be occupied by the probe (including its radius) and thus gives an estimate of the volume that could be filled by any atomic species.[50]

Figure 15 shows in pictorial form void volumes for samples **1** and **2** investigated in this work as well as their H-analogues **1-H** and **2-H** reported elsewhere.[25,29] In Figure 15 the voids are shown in green color while the yellow color represents space where rotation is restricted. The presented graphics explain the differences in molecular dynamics for fluorinated samples and their H-derivatives. It is worthy to remind that molecular motion, reorientation of aromatic groups in steroidal rotators **1-H** and **2-H**, was unambiguously proved.[25,29] It is apparent from analysis of data displayed in Figure 15 that the

https://dx.doi.org/10.1021/acs.cgd.9b01179
Cryst. Growth Des. 2020, 20, 2202−2216

precondition regarding free volume is not accomplished for **1** and **2**.

As we mentioned above as input files for analysis of voids, we have used the available single crystal X-ray data. The measured values of $^{1}H-^{13}C$ dipolar coupling and ^{13}C CSA are consistent with the observation that the free volume space in the crystal lattice of **2A** is larger than for **2B**. This space is sufficient for free rotation around the 1−4 axis whereas for **2B** not more than small amplitude wobbling can occur.

For **1**, the π-jump can only take place during phase transition as an individual "event" but not as continuing process. The case of not fluorinated molecules (**1-H** and **2-H**) is completely different. For both samples the aromatic rings are located in the green zone. This means that free volume in the neighborhood of the rotator guarantees its free rotation.

CONCLUSIONS

In this work we examined single crystal X-ray diffraction and high resolution solid state NMR spectroscopy data for acyclic and cyclic steroidal molecular rotors containing 1,4-diethynyl-2,3-difluoro-1,4-phenylene units as rotators with the aim to explain the correlation between the size of difluoro-phenylene units and free space in the crystal lattice required for molecular reorientation and further topology and time scale of dynamic processes. Our studies revealed that replacing hydrogen by fluorine atoms in acyclic rotors has significant consequences for dynamic processes. On the basis of NMR data, we concluded that there is no free rotation of fluorinated aromatic residues around the 1−4 axis in sample **1** in the kHz time scale. The only one large amplitude reorientation, so-called π-jump around the 1−4 axis was observed for acyclic sample **1** during the phase transition related with solvent migration from the crystal lattice. Analysis of $^{1}H-^{13}C$ dipolar couplings and ^{13}C CSA parameters showed that only very small, negligible amplitude wobbling is allowed in the crystal lattice of **1**. The X-ray structure examination proved that the free volume determined by crystal packing for **1** is not sufficient to allow unrestricted rotation of fluorinated aromatic residues in the unit cell.

The case of cyclic rotor **2** is significantly different. The first difference is related with the role of vinylene fragment which connects the steroidal units making this molecule cyclic. This residue is responsible for space reservation for difluoro-phenyl group. Such function which resemblances "umbrella effect" makes that the void, which is crucial for rotator motion for both crystallographic systems (**2A**, **2B**), is present although to a different extent. The presence of solvent in the crystal lattice of **2B** can be an additional factor reducing the voids and in consequence may restrict the molecular dynamics. For this reason difluoro-phenyl rotator for sample **2B** is wobbling with amplitude slightly larger compared to **1** but not freely rotating around the 1−4 axis. Such molecular motion was observed for sample **2A**. The phase transition and mechanism of thermal rearrangement **2B** → **2A** is very spectacular. It is a unique observation not only for steroidal rotators but we believe that for all species behaving as guest-controlled crystalline molecular machines.

Finally, we wish to highlight that such a complex nature of H-analogues of sample **1** and **2** was not observed. For H-analogues, conditions defining the size of voids in the crystal lattice and further the ability of systems for free rotation has been fulfilled. For **1** and **2** samples fulfilling this condition is not apparent.

ASSOCIATED CONTENT

Supporting Information

The Supporting Information is available free of charge at https://pubs.acs.org/doi/10.1021/acs.cgd.9b01179.

Synthetic procedures and full analysis of intermediate compounds; tables and figures of experimental and calculated NMR results as well as atomic coordinates used in GIPAW calculations (PDF)

Accession Codes

CCDC 1817202 and 1950550−1950551 contain the supplementary crystallographic data for this paper. These data can be obtained free of charge via www.ccdc.cam.ac.uk/data_request/cif, or by emailing data_request@ccdc.cam.ac.uk, or by contacting The Cambridge Crystallographic Data Centre, 12 Union Road, Cambridge CB2 1EZ, UK; fax: +44 1223 336033.

AUTHOR INFORMATION

Corresponding Authors

Tomasz Pawlak − *Centre of Molecular and Macromolecular Studies, Polish Academy of Sciences, 90-363 Lodz, Poland*; Email: tpawlak@cbmm.lodz.pl, tpawlak@wp.eu

Marek J. Potrzebowski − *Centre of Molecular and Macromolecular Studies, Polish Academy of Sciences, 90-363 Lodz, Poland*; orcid.org/0000-0001-5672-0638; Email: marekpot@cbmm.lodz.pl

Authors

Dorota Czajkowska-Szczykowska − *Faculty of Chemistry, University of Białystok, 15-245 Białystok, Poland*; orcid.org/0000-0002-7297-7422

Izabella Jastrzebska − *Faculty of Chemistry, University of Białystok, 15-245 Białystok, Poland*

Rosa Santillan − *Departamento de Química, Centro de Investigación y de Estudios Avanzados del IPN, Ciudad de México 07000, México*

Barbara Seroka − *Faculty of Chemistry, University of Białystok, 15-245 Białystok, Poland*

Jadwiga Maj − *Faculty of Chemistry, University of Białystok, 15-245 Białystok, Poland*

Jacek W. Morzycki − *Faculty of Chemistry, University of Białystok, 15-245 Białystok, Poland*; orcid.org/0000-0002-9049-5670

Pablo Labra-Vázquez − *Facultad de Química, Departamento de Química Orgánica, Universidad Nacional Autónoma de México, 04510 Ciudad de México, México*; orcid.org/0000-0002-8843-9709

Norberto Farfán − *Facultad de Química, Departamento de Química Orgánica, Universidad Nacional Autónoma de México, 04510 Ciudad de México, México*

Grzegorz D. Bujacz − *Institute of Technical Biochemistry, Faculty of Biotechnology and Food Sciences, Lodz University of Technology, 90-924 Lodz, Poland*

Complete contact information is available at: https://pubs.acs.org/10.1021/acs.cgd.9b01179

Notes

The authors declare no competing financial interest.

ACKNOWLEDGMENTS

The computational resources were partially provided by the Polish Infrastructure for Supporting Computational Science in the European Research Space (PL-GRID). Authors would like

to express their gratitude to PAIP (IN222819) for financial support. P.L-V. gratefully acknowledges a doctoral scholarship from CONACYT (337958).

REFERENCES

(1) Prokop, A.; Vacek, J.; Michl, J. Friction in Carborane-Based Molecular Rotors Driven by Gas Flow or Electric Field: Classical Molecular Dynamics. *ACS Nano* **2012**, *6*, 1901−1914.
(2) Rodríguez-Velamazán, J.; González, M. A.; Real, J. A.; Castro, M.; Muñoz, M. C.; Gaspar, A. B.; Ohtani, R.; Ohba, M.; Yoneda, K.; Hijikata, Y.; Yanai, N.; Mizuno, M.; Ando, H.; Kitagawa, S. A Switchable Molecular Rotator: Neutron Spectroscopy Study on a Polymeric Spin-Crossover Compound. *J. Am. Chem. Soc.* **2012**, *134*, 5083−5089.
(3) Coskun, A.; Banaszak, M.; Astumian, R. D.; Stoddart, J. F.; Grzybowski, B. A. Great Expectations: Can Artificial Molecular Machines Deliver on Their Promise? *Chem. Soc. Rev.* **2012**, *41*, 19−30.
(4) Garcia-Garibay, M. A. Molecular Machines: Nanoscale Gadgets. *Nat. Mater.* **2008**, *7*, 431−432.
(5) Garcia-Garibay, M. A. Molecular Crystals on the Move: From Single-Crystal-to-Single-Crystal Photoreactions to Molecular Machinery. *Angew. Chem., Int. Ed.* **2007**, *46*, 8945−8947.
(6) Vogelsberg, C. S.; Garcia-Garibay, M. A. Crystalline Molecular Machines: Function, Phase Order, Dimensionality, and Composition. *Chem. Soc. Rev.* **2012**, *41*, 1892−1910.
(7) Arcos-Ramos, R.; Rodriguez-Molina, B.; Gonzalez-Rodriguez, E.; Ramirez-Montes, P. I.; Ochoa, M. E.; Santillan, R.; Farfán, N.; Garcia-Garibay, M. A. Crystalline Arrays of Molecular Rotors with TIPS-Trityl and Phenolic-Trityl Stators Using Phenylene, 1,2-Difluorophenylene and Pyridine Rotators. *RSC Adv.* **2015**, *5*, 55201−55208.
(8) Arcos-Ramos, R.; Rodriguez-Molina, B.; Romero, M.; Méndez-Stivalet, J. M.; Ochoa, M. E.; Ramirez-Montes, P. I.; Santillan, R.; Garcia-Garibay, M. A.; Farfán, N. Synthesis and Evaluation of Molecular Rotors with Large and Bulky tert-Butyldiphenylsilyloxy-Substituted Trityl Stators. *J. Org. Chem.* **2012**, *77*, 6887−6894.
(9) van Delden, R. A.; ter Wiel, M. K. J.; Pollard, M. M.; Vicario, J.; Koumura, N.; Feringa, B. L. Unidirectional Molecular Motor on a Gold Surface. *Nature* **2005**, *437*, 1337−1340.
(10) Horinek, D.; Michl, J. Surface-Mounted Altitudinal Molecular Rotors in Alternating Electric Field: Single-Molecule Parametric Oscillator Molecular Dynamics. *Proc. Natl. Acad. Sci. U. S. A.* **2005**, *102*, 14175−14180.
(11) Skopek, K.; Gladysz, J. A. Syntheses of Gyroscope-Like Molecules via Three-Fold Ring Closing Metatheses of Bis(phosphine) Complexes *trans*-$L_yM(P((CH_2)_nCH{=}CH_2)_3)_2$, and Extensions to Bis(phosphite) Complexes *trans*-$Fe(CO)_3(P(O(CH_2)_nCH{=}CH_2)_3)_2$. *J. Organomet. Chem.* **2008**, *693*, 857−866.
(12) Scarso, A.; Onagi, H.; Rebek, J. Mechanically Regulated Rotation of a Guest in a Nanoscale Host. *J. Am. Chem. Soc.* **2004**, *126*, 12728−12729.
(13) Akutagawa, T.; Shitagami, K.; Nishihara, S.; Takeda, S.; Hasegawa, T.; Nakamura, T.; Hosokoshi, Y.; Inoue, K.; Ikeuchi, S.; Miyazaki, Y.; Saito, K. Molecular Rotor of C_{s2}(18]crown-6)$_3$ in the Solid State Coupled with the Magnetism of [Ni(dmit)$_2$]. *J. Am. Chem. Soc.* **2005**, *127*, 4397−4402.
(14) Jian, H.; Tour, J. M. En Route to Surface-Bound Electric Field-Driven Molecular Motors. *J. Org. Chem.* **2003**, *68*, 5091−5103.
(15) Kottas, G. S.; Clarke, L. I.; Horinek, D.; Michl, J. Artificial Molecular Rotors. *Chem. Rev.* **2005**, *105*, 1281−1376.
(16) Browne, W. R.; Feringa, B. L. Making Molecular Machines Work. *Nat. Nanotechnol.* **2006**, *1*, 25−35.
(17) Skopek, K.; Hershberger, M. C.; Gladysz, J. A. Gyroscopes and the Chemical Literature: 1852−2002. *Coord. Chem. Rev.* **2007**, *251*, 1723−1733.
(18) Kay, E. R.; Leigh, D. A.; Zerbetto, F. Synthetic Molecular Motors and Mechanical Machines. *Angew. Chem., Int. Ed.* **2007**, *46*, 72−191.
(19) Pease, A. R.; Jeppesen, J. O.; Stoddart, J. F.; Luo, Y.; Collier, P. C.; Heath, J. R. Switching Devices Based on Interlocked Molecules. *Acc. Chem. Res.* **2001**, *34*, 433−444.
(20) Leigh, D. A.; Wong, J. K. Y.; Dehez, F.; Zerbetto, F. Unidirectional Rotation in a Mechanically Interlocked Molecular Rotor. *Nature* **2003**, *424*, 174−179.
(21) Karim, A. R.; Linden, A.; Baldridge, K. K.; Siegel, J. S. Symmetry and Polar-π Effects on the Dynamics of Enshrouded Aryl-Alkyne Molecular Rotors. *Chem. Sci.* **2010**, *1*, 102−110.
(22) Bracco, S.; Beretta, M.; Cattaneo, A.; Comotti, A.; Falqui, A.; Zhao, K.; Rogers, C.; Sozzani, P. Dipolar Rotors Orderly Aligned in Mesoporous Fluorinated Organosilica Architectures. *Angew. Chem., Int. Ed.* **2015**, *54*, 4773−4777.
(23) Bracco, S.; Castiglioni, F.; Comotti, A.; Galli, S.; Negroni, M.; Maspero, A.; Sozzani, P. Ultrafast Molecular Rotors and Their CO_2 Tuning in MOFs with Rod-Like Ligands. *Chem.-Eur. J.* **2017**, *23*, 11210−11215.
(24) Bracco, S.; Miyano, T.; Negroni, M.; Bassanetti, I.; Marchio, L.; Sozzani, P.; Tohnai, N.; Comotti, A. CO_2 Regulates Molecular Rotor Dynamics in Porous Materials. *Chem. Commun.* **2017**, *53*, 7776−7779.
(25) Rodriguez-Molina, B.; Farfán, N.; Romero, M.; Méndez-Stivalet, J. M.; Santillan, R.; Garcia-Garibay, M. A. Anisochronous Dynamics in a Crystalline Array of Steroidal Molecular Rotors: Evidence of Correlated Motion within 1D Helical Domains. *J. Am. Chem. Soc.* **2011**, *133*, 7280−7283.
(26) Rodriguez-Molina, B.; Ochoa, Ma. E.; Romero, M.; Khan, S. I.; Farfán, N.; Santillan, R.; Garcia-Garibay, M. A. Conformational Polymorphism and Isomorphism of Molecular Rotors with Fluoroaromatic Rotators and Mestranol Stators. *Cryst. Growth Des.* **2013**, *13*, 5107−5115.
(27) Jiménez-Garcia, C.; Arcos-Ramos, R.; Méndez-Stivalet, J. M.; Santillan, R.; Farfán, N. Synthesis and Characterization of Dissymmetric Molecular Rotors Based on 1,4-Diethynylphenylene Rotators and Steroidal/Trityl Type Stators. *Monatsh. Chem.* **2015**, *146*, 1005−1013.
(28) Rodriguez-Molina, B.; Pozos, A.; Cruz, R.; Romero, M.; Flores, B.; Farfán, N.; Santillan, R.; Garcia-Garibay, M. A. Synthesis and Solid State Characterization of Molecular Rotors with Steroidal Stators: Ethisterone and Norethisterone. *Org. Biomol. Chem.* **2010**, *8*, 2993−3000.
(29) Jastrzebska, I.; Pawlak, T.; Arcos-Ramos, R.; Florez-Lopez, E.; Farfan, N.; Czajkowska-Szczykowska, D.; Maj, J.; Santillan, R.; Morzycki, J. W.; Potrzebowski, M. J. Synthesis, Structure, and Local Molecular Dynamics for Crystalline Rotors Based on Hecogenin/Botogenin Steroidal Frameworks. *Cryst. Growth Des.* **2016**, *16*, 5698−5709.
(30) Mayorquin-Torres, M. C.; Colin-Molina, A.; Perez-Estrada, S.; Galano, A.; Rodriguez-Molina, B.; Iglesias-Arteaga, M. A. Synthesis, Characterization, and Solid State Dynamic Studies of a Hydrogen Bond-Hindered Steroidal Molecular Rotor with a Flexible Axis. *J. Org. Chem.* **2018**, *83*, 3768−3779.
(31) Dolomanov, O. V.; Bourhis, L. J.; Gildea, R. J.; Howard, J. A. K.; Puschmann, H. *J. Appl. Crystallogr.* **2009**, *42*, 339.
(32) Sheldrick, G. A Short History of SHELX. *Acta Crystallogr., Sect. A: Found. Crystallogr.* **2008**, *64*, 112−122.
(33) Farrugia, L. J. WinGX Suite for Small-Molecule Single-Crystal Crystallography. *J. Appl. Crystallogr.* **1999**, *32*, 837−838.
(34) Macrae, C. F.; Edgington, P. R.; McCabe, P.; Pidcock, E.; Shields, G. P.; Taylor, R.; Towler, M.; van de Streek, J. Mercury: Visualization and Analysis of Crystal Structures. *J. Appl. Crystallogr.* **2006**, *39*, 453−457.
(35) Farrugia, L. J. ORTEP-3 for Windows - a version of ORTEP-III with a Graphical User Interface (GUI). *J. Appl. Crystallogr.* **1997**, *30*, 565.
(36) Morcombe, C. R.; Zilm, K. W. Chemical Shift Referencing in MAS Solid State NMR. *J. Magn. Reson.* **2003**, *162*, 479−486.

https://dx.doi.org/10.1021/acs.cgd.9b01179
Cryst. Growth Des. 2020, 20, 2202−2216

(37) Metz, G.; Wu, X.; Smith, S. O. Ramped-Amplitude Cross Polarization in Magic-Angle-Spinning NMR. *J. Magn. Reson., Ser. A* **1994**, *110*, 219−227.
(38) Bennett, A. E.; Rienstra, C. M.; Auger, M.; Lakshmi, K. V.; Griffin, R. G. Heteronuclear Decoupling in Rotating Solids. *J. Chem. Phys.* **1995**, *103*, 6951−6958.
(39) Dvinskikh, S. V.; Sandström, D. Frequency Offset Refocused PISEMA-type Sequences. *J. Magn. Reson.* **2005**, *175*, 163−169.
(40) Antzutkin, O. N.; Shekar, S. C.; Levitt, M. H. Two-Dimensional Sideband Separation in Magic-Angle-Spinning NMR. *J. Magn. Reson., Ser. A* **1995**, *115*, 7−19.
(41) *TopSpin*, v. 3.0; Bruker BioSpin GmbH, Karlsruhe, Germany.
(42) Mao, K.; Wiench, J. W.; Lin, V. S.-Y.; Pruski, M. Indirectly Detected Through-Bond Chemical Shift Correlation NMR Spectroscopy in Solids under Fast MAS: Studies of Organic−Inorganic Hybrid Materials. *J. Magn. Reson.* **2009**, *196*, 92−95.
(43) Ishii, Y.; Tycko, R. Sensitivity Enhancement in Solid State ^{15}N NMR by Indirect Detection with High-Speed Magic Angle Spinning. *J. Magn. Reson.* **2000**, *142*, 199−204.
(44) Clark, S. J.; Segall, M. D.; Pickard, C. J.; Hasnip, P. J.; Probert, M. I. J.; Refson, K.; Payne, M. C. First Principles Methods Using CASTEP. *Z. Kristallogr. - Cryst. Mater.* **2005**, *220*, 567−570.
(45) Segall, M. D.; Lindan, P. J. D.; Probert, M. J.; Pickard, C. J.; Hasnip, P. J.; Clark, S. J.; Payne, M. C. First-Principles Simulation: Ideas, Illustrations and the CASTEP Code. *J. Phys.: Condens. Matter* **2002**, *14*, 2717−2744.
(46) Perdew, J. P.; Burke, K.; Ernzerhof, M. Generalized Gradient Approximation Made Simple. *Phys. Rev. Lett.* **1996**, *77*, 3865−3868.
(47) Vanderbilt, D. Soft Self-Consistent Pseudopotentials in a Generalized Eigenvalue Formalism. *Phys. Rev. B: Condens. Matter Mater. Phys.* **1990**, *41*, 7892−7895.
(48) Monkhorst, H. J.; Pack, J. D. Special Points for Brillouin-Zone Integrations. *Phys. Rev. B* **1976**, *13*, 5188−5192.
(49) Nocedal, J.; Wright, S. J. *Numerical Optimization*; Springer-Verlag: New York, 2006; second ed.
(50) Macrae, C. F.; Bruno, I. J.; Chisholm, J. A.; Edgington, P. R.; McCabe, P.; Pidcock, E.; Rodriguez-Monge, L.; Taylor, R.; van de Streek, J.; Wood, P. A. Mercury CSD 2.0 − New Features for the Visualization and Investigation of Crystal Structures. *J. Appl. Crystallogr.* **2008**, *41*, 466−470.
(51) Dudek, M. K.; Kazmierski, S.; Kostrzewa, M.; Potrzebowski, M. J. Solid-State NMR Studies of Molecular Crystals. *Annu. Rep. NMR Spectrosc.* **2018**, *95*, 1−81.
(52) Jeziorna, A.; Kazmierski, S.; Paluch, P.; Skorupska, E.; Potrzebowski, M. J. Recent Progress in the Solid-State NMR Studies of Short Peptides: Techniques, Structure and Dynamics. *Annu. Rep. NMR Spectrosc.* **2014**, *83*, 67−143.
(53) Bielecki, A.; Kolbert, A. C.; Levitt, M. H. Frequency-Switched Pulse Sequences: Homonuclear Decoupling and Dilute Spin NMR in Solids. *Chem. Phys. Lett.* **1989**, *155*, 341−346.
(54) Vasa, S. K.; Rovó, P.; Linser, R. Protons as Versatile Reporters in Solid-State NMR Spectroscopy. *Acc. Chem. Res.* **2018**, *51*, 1386−1395.
(55) Pawlak, T.; Paluch, P.; Trzeciak-Karlikowska, K.; Jeziorna, A.; Potrzebowski, M. J. Study of the Thermal Processes in Molecular Crystals of Peptides by Means of NMR Crystallography. *CrystEngComm* **2013**, *15*, 8680−8692.
(56) Dudek, M. K.; Pawlak, T.; Paluch, P.; Jeziorna, A.; Potrzebowski, M. J. A Multi-Technique Experimental and Computational Approach to Study the Dehydration Processes in the Crystals of Endomorphin Opioid Peptide Derivative. *Cryst. Growth Des.* **2016**, *16*, 5312−5322.
(57) Brown, S. P. Applications of High-Resolution ^{1}H Solid-State NMR. *Solid State Nucl. Magn. Reson.* **2012**, *41*, 1−27.
(58) Zhang, R.; Mroue, K. H.; Ramamoorthy, A. Proton-Based Ultrafast Magic Angle Spinning Solid-State NMR Spectroscopy. *Acc. Chem. Res.* **2017**, *50*, 1105−1113.
(59) Rodríguez-Molina, B.; Pérez-Estrada, S.; Garcia-Garibay, M. A. Amphidynamic Crystals of a Steroidal Bicyclo[2.2.2]octane Rotor: A High Symmetry Group That Rotates Faster than Smaller Methyl and Methoxy Groups. *J. Am. Chem. Soc.* **2013**, *135*, 10388−10395.
(60) Czajkowska-Szczykowska, D.; Rodríguez-Molina, B.; Magaña-Vergara, N. E.; Santillan, R.; Morzycki, J. W.; Garcia-Garibay, M. A. Macrocyclic Molecular Rotors with Bridged Steroidal Frameworks. *J. Org. Chem.* **2012**, *77*, 9970−9978.
(61) Krushelnitsky, A.; Reichert, D. Solid-state NMR and protein dynamics. *Prog. Nucl. Magn. Reson. Spectrosc.* **2005**, *47*, 1−25.
(62) Schanda, P.; Ernst, M. Studying Dynamics by Magic-Angle Spinning Solid-State NMR Spectroscopy: Principles and Applications to Biomolecules. *Prog. Nucl. Magn. Reson. Spectrosc.* **2016**, *96*, 1−46.
(63) Reichert, D.; Saalwachter, K. *Dipolar Recoupling: Molecular-level Mobility in NMR Chystallography*; Harris, R. K., Wasylishen, R. E., Duer, M. J., Eds.; Wiley and Sons Ltd.: UK, 2009.
(64) Dvinskikh, S. V.; Zimmermann, H.; Maliniak, A.; Sandström, D. Heteronuclear Dipolar Recoupling in Liquid Crystals and Solids by PISEMA-type Pulse Sequences. *J. Magn. Reson.* **2003**, *164*, 165−170.
(65) Alderman, D. W.; McGeorge, G.; Hu, J. Z.; Pugmire, R. J.; Grant, D. M. A sensitive, high resolution magic angle turning experiment for measuring chemical shift tensor principal values. *Mol. Phys.* **1998**, *95*, 1113−1126.
(66) Frydman, L.; Chingas, G. C.; Lee, Y. K.; Grandinetti, P. J.; Eastman, M. A.; Barrall, G. A.; Pines, A. Variable-angle correlation spectroscopy in solid-state nuclear magnetic resonance. *J. Chem. Phys.* **1992**, *97*, 4800−4808.
(67) Antzutkin, O. N.; Shekar, S. C.; Levitt, M. H. J. Two-dimensional sideband separation in magic-angle-spinning NMR. *J. Magn. Reson., Ser. A* **1995**, *115*, 7−19.
(68) Pawlak, T.; Trzeciak-Karlikowska, K.; Czernek, J.; Ciesielski, W.; Potrzebowski, M. J. Computed and Experimental Chemical Shift Parameters for Rigid and Flexible YAF Peptides in the Solid State. *J. Phys. Chem. B* **2012**, *116*, 1974−1983.
(69) Alkan, F.; Holmes, S. T.; Dybowski, C. Role of Exact Exchange and Relativistic Approximations in Calculating 19F Magnetic Shielding in Solids Using a Cluster Ansatz. *J. Chem. Theory Comput.* **2017**, *13*, 4741−4752.
(70) Paluch, P.; Pawlak, T.; Amoureux, J.-P.; Potrzebowski, M. J. Simple and Accurate Determination of X−H Distances under Ultra-Fast MAS NMR. *J. Magn. Reson.* **2013**, *233*, 56−63.
(71) Paluch, P.; Pawlak, T.; Jeziorna, A.; Trébosc, J.; Hou, G.; Vega, A. J.; Amoureux, J.-P.; Dracinsky, M.; Polenova, T.; Potrzebowski, M. J. Analysis of Local Molecular Motions of Aromatic Sidechains in Proteins by 2D and 3D Fast MAS NMR Spectroscopy and Quantum Mechanical Calculations. *Phys. Chem. Chem. Phys.* **2015**, *17*, 28789−28801.

https://dx.doi.org/10.1021/acs.cgd.9b01179
Cryst. Growth Des. 2020, 20, 2202−2216